ROYAL SOCIETY OF CHEMISTRY

Check for updates

Analcime zeolite synthesis from the bottom ash of co-incinerated industrial hazardous and medical waste for tetracycline removal from wastewater

Anhong Li,[a] Ping Li,[b] Xiaolin Yue,[b] Zehua Huang,[c] Jing Zhang,[b] Wenyuan Tan [ID][b] and Dong Yuan [ID] *[a]

Bottom ash (BA) produced from the centralized incineration of industrial hazardous waste and medical waste is a hazardous solid waste. Therefore, although challenging, it is necessary to develop recycling technologies that can convert BA into useful products. In this study, we developed a method for the preparation of analcime zeolite (ANA) *via* a BA acid leaching−melting−hydrothermal method. Unlike the existing method that involves using fly ash *via* a hydrothermal technology to synthesize mixed zeolites, such as NaPI zeolite ($NaAl_6Si_{10}O_{12} \cdot 12H_2O$), tobermorite ($Ca_5Si_6(OH)_2O_{16} \cdot 4H_2O$), sodalite ($Na_4Al_3Si_3O_{12}Cl$) and ANA ($NaAlSi_2O_6 \cdot H_2O$), the acid leaching−melting−hydrothermal method was used to synthesize pure ANA. ANA has application potential in the adsorption of wastewater pollutants. Herein, the synthesized ANA was used as an adsorbent to adsorb tetracycline (TC), ciprofloxacin (CIP), norfloxacin (NOR) and enrofloxacin (ENR) in water. Results of this study showed that ANA with a low impurity content could be synthesized using BA as the starting material. The adsorption capacities of ANA for TC, CIP, NOR and ENR were 134.2 mg g^{-1}, 64.3 mg g^{-1}, 56.5 mg g^{-1} and 43.8 mg g^{-1}, respectively. The adsorption process of TC by ANA was studied. It was found that the optimal conditions were an adsorbent dose of 0.4 g L^{-1}, pH = 7, and a contact time of 300 min. The maximum adsorption capacity was 936.86 mg g^{-1}, which was much higher than the adsorption capacity of the existing zeolite for TC. The kinetic and isotherm fitting data showed that the adsorption of TC on ANA mainly involved monolayer chemical adsorption, and the process was more in line with the pseudo-second-order kinetic model and the Langmuir isotherm adsorption model. These results confirm that ANA is an efficient and economical TC adsorbent.

Introduction

With the rapid development of society, the production of industrial hazardous waste[1] and medical waste[2] has increased dramatically. The improper treatment of industrial hazardous waste and medical waste can easily cause disease transmission and pollution, posing huge threats to the environment.[3–5] At present, industrial hazardous waste and medical waste are mainly incinerated in incineration plants,[6] leaving behind about 80% bottom ash (BA).[7] According to the existing reports, fly ash can be widely recycled. Compared with BA, it has a higher yield, more complex components and lower toxicity.[8–11] Therefore, BA has a higher potential for resource utilization. However, BA is classified as hazardous waste because it contains toxic substances (such as heavy metals). During conventional treatment, BA is usually dumped in landfills, which can lead to

the leaching of heavy metals and pose a risk to the environment (soil, surface water, and groundwater).[12,13]

In the existing literature, BA is mostly used to make building materials (such as the production of aggregates in cement stabilized macadam,[14,15] backfill materials,[16] mixed cement,[17] concrete,[18,19] and microcrystalline glass[20]), and there is a risk of heavy metal precipitation. In recent years, the conversion of waste into adsorbents to improve the environment has provided a promising option for alleviating the strain on natural resources and the environment.[21] Among such wastes, the use of BA to synthesize zeolites not only offers the advantages of stabilizing a variety of heavy metals, small volume change before and after treatment, and simple operation[22] but also exhibits good ion-exchange, adsorption and catalysis abilities, acid and alkali resistances and thermal stability, along with high economic and practical value.[23,24]

With the rapid growth of the economy, there is an increasing demand for improved medical care, hygiene and food safety, which has led to the widespread use of antibiotics. Large quantities of antibiotics are released into the environment, leading to a growing problem of antibiotic pollution.[25] Antibiotic pollution exists not only in water bodies, but also in soil, air

[a] College of Chemistry and Environment Engineering, Sichuan University of Science & Engineering, Zigong, Sichuan, 643000, China. E-mail: yuandong68@126.com

[b] College of Chemistry Engineering, Sichuan University of Science & Engineering, Zigong, Sichuan, 643000, China

[c] Beijing SPC Environment Protection Tech Co., Ltd, Beijing, China

and agricultural products, posing a serious threat to human health and the ecological environment, and further endangering sustainable economic and social development.[26] There is a strong link between economic development and environmental protection,[27] and to ensure human health and the sustainable development of the ecological environment, there is an urgent need to take effective measures to reduce and effectively deal with the pollution of antibiotics.

In this study, BA was converted into an analcime zeolite (ANA) adsorbent material with a high utilization value by a hydrothermal synthesis method. Different from the mixed zeolite synthesized by the existing hydrothermal method, the hydrothermal method can be used to synthesize pure analcime zeolite in a reduced synthesis time. It was applied here to simulate the removal of tetracycline (TC), ciprofloxacin (CIP), norfloxacin (NOR) and enrofloxacin (ENR) from wastewater to achieve the purpose of treating waste with waste, thus improving the comprehensive utilization value of BA as well as providing a feasible technical route for solving the problem of antibiotic water pollution.

Experimental section

Materials and chemical reagents

BA was sourced from Xinjiang Jinpai Environmental Technology Co., Ltd. Hydrochloric acid (HCl, 37%), sodium hydroxide (NaOH, ≥98%) and potassium fluoride (KF, 99.99%) were purchased from Macklin Chemical Reagent Co Ltd (Shanghai, China). Tetracycline (TC, $C_{22}H_{24}N_2O_8$), ciprofloxacin (CIP, $CHFN_3O_3$), norfloxacin (NOR, $C_{16}H_{18}FN_3O_3$) and enrofloxacin (ENR, $C_{19}H_{22}FN_3O_3$) were obtained from Adamas Chemicals Co Ltd (Shanghai, China). All the chemicals were used without further purification.

Methods

Synthesis of analcime. The flowchart for the synthesis of analcime from BA is presented in Fig. 1. First, BA was reacted with 4 mol per L HCl at 90 °C for 2 h (solid–liquid ratio of 1 : 5), and then separated as a solid–liquid by centrifuge, and dried at 105 °C for 24 h. After drying, the product was mixed with NaOH

Fig. 1 Flowchart for the synthesis of analcime from BA.

to obtain a gray-alkali mixture (ash-alkali ratio of 2 : 1), which was placed in a nickel boat and heated to 550 °C and maintained there for 1 h. Afterwards, the mixture was cooled to room temperature and then taken out, and the obtained molten product was called molten ash. Next, the molten ash and deionized water were placed in a reaction kettle (solid–liquid ratio of 1 : 4) and reacted at 180 °C for 4–12 h. The solid samples were dried at 105 °C for 24 h to obtain the analcime zeolite sample. The phase purity of the synthesized ANA was determined from the corresponding XRD patterns of the phase-pure samples.

Adsorption of antibiotics. Calculated amounts of antibiotics (TC, CIP, NOR and ENR) were dissolved in deionized water to obtain solution concentrations of 100 and 20 mg L^{-1}, respectively. The pH of the exchange solution was set to neutral (7 ± 0.2) by adjusting the solution with 0.01 M HCl and 0.01 M NaOH solutions. The adsorption experiments were performed in a temperature shaker for 24 h (at R.T. 25 ± 1 °C, adding 50 mL TC, CIP, NOR and ENR solution) to 20 mg ANA, respectively.

The equilibrium adsorption capacity (Q_e) and treatment efficiency ($T\%$) were calculated from eqn (1) and (2).

$$Q_e = [(C_0 - C_e)V]/M \qquad (1)$$

$$T\% = [(C_0 - C_e)/C_0 \times 100] \qquad (2)$$

where Q_e (mg g^{-1}) is the adsorption capacity, T (%) is the treatment efficiency, C_0 (mg L^{-1}) is the initial TC concentration, C_e (mg L^{-1}) is the residual TC concentration, V (mL) is the aqueous solution volume and M (mg) is the mass of the adsorbent.

Instrumentation and characterization techniques. The elemental composition of BA was determined by X-ray fluorescence spectrometry (Panaco Zetium, the Netherlands). The phase and crystal structure of BA and the synthesized phases of ANA products were determined using by X-ray diffraction (XRD; Germany Bruker, D2PHASER). The topography, composition, and structure of the sample surface were determined by field emission scanning electron microscopy (FESEM; Hitachi, SEM5000). A V-Sorb-2802-TP surface area analyzer was used to measure the Brunauer–Emmet–Teller (BET) surface area and corresponding pore volume. The particle sizes of the samples were analyzed using an NKT6100-D particle-size analyzer. FT-IR data were collected from 4000 cm^{-1} to 400 cm^{-1} in transmission mode using a Thermo Nicolet iS5 instrument with a resolution of 4 cm^{-1}. Thermogravimetric (TG) and differential thermal analysis (DTA) were performed on 10–20 mg samples using a SETSYS Evolution model TG-DTA instrument (Setaram, France). Antibiotics concentrations were determined by ultraviolet-visible spectrophotometry (UV-vis; UV-1700PC).

Results and discussion

Characterization of the experimental products

The major and trace elements in the samples were determined by XRF, as shown in Table 1. BA contained CaO, Al_2O_3, SiO_2. The SiO_2 content was 12.718% and the ratio of Si/Al in this BA was
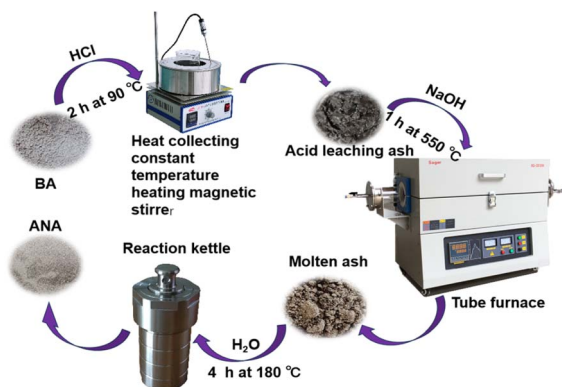
Table 1 Major and trace elements in the samples obtained using XRF and their masses

Element compositions (simple substance forms)	BA		Acid-leached ash		Molten ash	
	wt%	Mass (mg)	wt%	Mass (mg)	wt%	Mass (mg)
Ca	23.824	4764.8	27.336	1011.432	11.432	571.6
Cl	6.412	1282.4	13.33	493.21	7.844	392.2
Na	6.23	1246	1.354	50.098	38.836	1941.8
Si	4.846	969.2	30.244	1119.028	20.035	1001.75
Al	1.637	327.4	2.091	77.367	1.5	75
Fe	1.36	272	3.491	129.167	0.97	48.5
Ti	0.946	189.2	0.519	19.203	0.153	7.65
F	0.692	138.4	—	—	—	—
Mg	0.385	77	0.241	8.917	0.139	0.695
K	0.267	53.4	0.255	9.435	0.167	8.35
Ce	0.048	9.6	—	—	—	—

2.96, which is an ideal composition for the synthesis of zeolites.[28–31] Although the content of heavy metals in BA was small, the variety was considerable. It was necessary to pretreat BA to prevent the precipitation of heavy metals in the synthetic zeolite. After acid treatment, 20 g of BA was converted into 3.7 g of acid-leached ash, and then 5 g of molten ash was be further obtained by alkaline treatment. The XRF element mass ratios were analyzed, and the calculation results for the element masses are shown in Table 1. The acid treatment method could significantly remove most of the impurities, including Ca, Cl, Fe, F and Ce. Alkali treatment could further remove some elements such as Ca, Cl, Fe, and Ti.

Next, the physical phase and chemical composition of the BA, acid-treated ash and molten ash were investigated by XRD and the results are presented in Fig. 2a. The XRD pattern of BA showed diffraction peaks associated with quartz, along with peaks for NaCl, $CaCO_3$ and $Ca(OH)_2$. However, the diffraction peak intensities of NaCl, $CaCO_3$ and $Ca(OH)_2$ in BA became weakened or even disappeared after the samples were treated with acid. Moreover, alkali treatment introduced NaOH, while retaining $Al(OH)_3$ and SiO_2 for the subsequent synthesis of higher-purity analcime zeolites. The alkali treatment converted insoluble quartz into more soluble amorphous silica, which improved its solubility and consequently the rate of zeolite formation.[32]

The alkali-treated fly ash was hydrothermally reacted at 180 °C for 4–12 h, as shown in Fig. 2b. The synthetic ANA displayed eight distinct XRD diffraction peaks located at 15.84°, 18.30°,

25.99°, 30.58°, 33.31°, 35.88°, 47.80°, and 52.53°, corresponding to the (211), (220), (400), (332), (431), (521), (640), and (651) crystal planes of the standard card of ANA (PDF#41-1478), respectively. The characteristic diffraction peaks corresponding to analcime zeolite appeared in all samples after 4–12 h hydrothermal reaction. The formation of analcime zeolite could be achieved after 4 h hydrothermal treatment. In the observed diffraction peaks (e.g., 15.84° and 25.99°), the intensity of some peaks slightly increased with prolonging the hydrothermal synthesis time. Simultaneously, certain impurity peaks (e.g., 27.8° and 29.3°) showed a mild reduction in intensity with extending the synthesis time. Considering both the synthesis cost and efficiency of analcime (ANA), this study ultimately selected 4 h as the optimal hydrothermal synthesis duration.

The microstructure, chemical composition, and size of the samples were characterized by SEM, as illustrated in Fig. 3. As illustrated in Fig. 3a, BA was in the form of large lumps with no special morphology, but following acid treatment, BA became smaller in size and displayed a dispersed porous structure (Fig. 3b). The surface became dense and smooth when further activated by NaOH at high temperature (Fig. 3c), which was due to the transformation of SiO_2 into an amorphous glassy phase
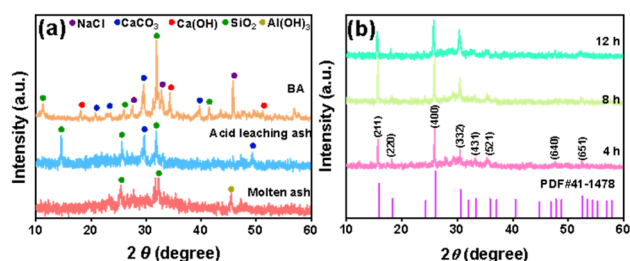

Fig. 2 XRD patterns of the (a) experimental products and (b) analcime zeolite synthesized at increasing hydrothermal reaction times.
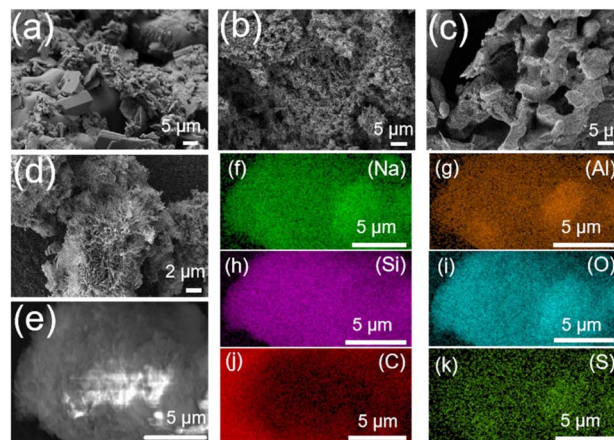

Fig. 3 SEM images of BA (a), acid-leached ash (b), molten ash (c) and ANA (d and e) and EDS elemental mapping of ANA (f–k).
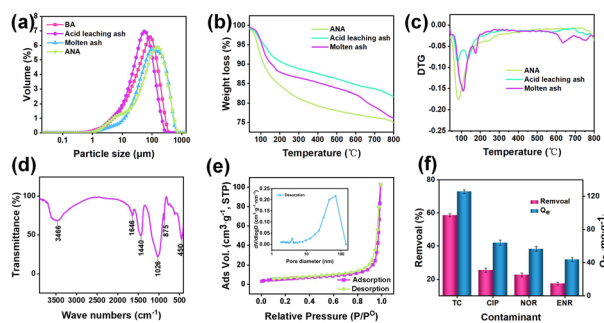
Fig. 4 Particle-size distribution of the samples (a), DTA-TG analysis of the samples (b and c), FT-IR spectrum of ANA (d), BET surface area measurement using nitrogen adsorption–desorption isotherms (e), and adsorption capacity of ANA for antibiotics (f) (the initial concentration of contaminants was 100 mg L^{-1}).

during alkali fusion, making it easier to dissolve in the hydrothermal solution. ANA had a flower-like and needle-like three-dimensional structure (Fig. 3d and e). The EDS scanning image displayed the presence of various elements on the ANA surface, including Na, Al, Si, O, C, and S (Fig. 3f).

The particle-size distributions of the experimental products are illustrated in Fig. 4a. The particle-size-distribution curves for BA, acid-treated ash and molten ash all showed a single-peak distribution with peaks at 87.4, 54.7 and 102.2 μm, respectively. In contrast, ANA showed a bimodal distribution, with peak maxima at 7.1 and 139.8 μm. The results of the particle-size analysis are listed in Table 2. The smaller particle-size distribution of the acid-leached ash was due to the dispersion of crystals as a result of the acidolytic reaction. The larger particle size of the molten ash was due to the heating of NaOH and the higher reaction temperature, which caused some of the solids to melt and agglomerate.

Thermogravimetric analysis was performed on the ANA, acid-treated ash, and molten ash. The thermogravimetric curves for heating from 50 °C to 800 °C under a N_2 atmosphere are presented in Fig. 4b and c, with a gradual loss of moisture. The DTA-TG curves showed three weight loss peaks at 80.8 °C, 135.1 °C and 573.7 °C for the acid-treated ash and four weight loss peaks at 109.3 °C, 174.1 °C, 635.7 °C and 753.8 °C for the alkali-treated ash. In particular, two significant dehydration episodes were observed at 85 °C and 231 °C for ANA. After the temperature was increased to 300 °C the curve became smoother and the sample stabilized. Since no organic materials were present in the sample, the first two losses should

correspond to the removal of physically adsorbed water and occluded water from the sample, respectively. The weight loss peak of the acid-leached ash at 573.7 °C was caused by the decomposition of residual calcium carbonate,[33] and the weight loss peaks of molten ash at 635.7 °C and 753.8 °C were pyrolysis reactions of NaOH.[34] The synthesized ANA was quite stable at high temperature, which proved that the ANA has good thermal stability.

The total weight losses of the acid-leached ash, molten ash and ANA were 18.4%, 24.0% and 25.04%, respectively. The weight loss of ANA mainly appeared at 100 °C, which was caused by the evaporation of physically adsorbed water. The results indicated that analcime zeolite could adsorb more water molecules and store them in its porous structure. The water absorption was related to the number of pores in the specimen, and based on their SEM images, it was evident that the acid-leached ash and molten ash with dense and smooth surfaces lacked a porous structure, while ANA possessed a flower-like structure with dense pores.

Information related to the chemical bonds or functional groups in the ANA was obtained using FT-IR spectroscopy, as illustrated in Fig. 4d. The data shown are similar to those in the literature, indicating that the synthesized material was a relatively pure analcime zeolite.[35] The absorption peaks for O–H stretching and bending were located at 3466 and 1646 cm^{-1}, respectively.[36] In particular, the band at 3466 cm^{-1} was associated with the asymmetric stretching mode of water coordinated at the pore edge, while the band at 1646 cm^{-1} was attributed to zeolite water in the zeolite pore.[37] The band located at 1026 cm^{-1} was attributed to the O–Na–O stretching mode, while the bands located at 875 and 450 cm^{-1} were attributed to the Si–O–Si symmetric stretching vibration, and the symmetric stretching vibration of the four-membered ring.[38]

Fig. 4e illustrates the N_2 adsorption–desorption isotherm for ANA at 77 K. Zeolites are typical microporous materials with a pore size of less than 2 nm, but in this study, the BET adsorption isotherm did not show steep nitrogen uptake at low P/P^O, indicating the lack of a type I adsorption behavior in ANA. As a result, ANA showed little or no microporous structure. ANA pore sizes in the range of 2–50 nm corroborated those of typical mesopores showing a type IV behavior.[39] The specific surface area of ANA was 20 m^2 g^{-1}. The vertical H3-type hysteresis loops in ANA greater than 0.9 (P/P_o) suggested that the pores may be slit-like.[40] The pore-size-distribution curves (dV/d log D curves) of ANA presented a mesopores distribution of 2–50 nm and a macropores distribution of 50–200 nm. The studied ANA

Table 2 Data from the particle-size analysis

Experimental products	Particle-size diameter (μm)			Volume weighted mean D [3, 4]	Weight specific surface S/g (m² kg⁻¹)
	d_{10}	d_{50}	d_{90}		
BA	8.4	52.2	148.9	67.1	89.8
Acid-leached ash	8.0	40.5	110.5	51.4	92.2
Molten ash	16.6	87.9	281.2	121.8	54.0
ANA	9.3	89.6	282.2	121.6	70.1

Table 3 TC removal by different adsorbents

Adsorbent	Q_{max} (mg g^{-1})	Adsorbent dose (g L^{-1})	Ref.
Calcium-modified corn stover biochar	33.53	1.0	41
Ferroferric oxide nanoparticle-assisted powdered activated carbon	199.25	0.5	42
Fe–N modification biochars	156.00	1.0	43
Hydrochar thermally activated in air + N$_2$ at 500 °C	196.70	1.0	44
ANA	936.86	0.4	This work

possessed pores distributed in the range of 35 nm and 10–140 nm.

ANA adsorption of antibiotics

The adsorption rate of ANA for antibiotics is shown in Fig. 4f. The adsorption efficiencies of the synthesized analcime for TC, CIP, NOR and ENR (100 mg L^{-1} 50 mL) were 53.7%, 25.5%, 22.6% and 17.4%, respectively. The adsorption capacities for TC, CIP, NOR and ENR (100 mg L^{-1}, 50 mL) were 134.2, 63.8, 56.5, 43.5 mg g^{-1}, respectively. ANA has a high adsorption capacity for antibiotics and can adsorb a variety of pollutants. ANA prepared from BA can be widely used in medical wastewater treatment. The recycling and resource utilization of hazardous waste could thus be realized.

Compared with other adsorbents in previous studies, it was found that the adsorption capacity of TC on ANA was significantly higher than that on other reported adsorbents (Table 3). Despite using small quantities of ANA adsorbent, it demonstrated a large adsorption capacity, and its potential as an adsorbent. ANA had excellent TC adsorption performance, so ANA was selected to adsorb TC in the adsorption kinetics and isotherm studies.

Effect of the adsorbent dose and pH

Fig. 5a shows the effect of the ANA dose on TC. With the increase in dose, the removal efficiency of TC also increased.

Fig. 5 Effect of adsorbent dose (a) and pH (b) on the adsorption of TC, and the zeta potential of ANA (c).

When the dose of ANA was increased from 0.2 to 2 g L^{-1}, the adsorption rate of TC increased rapidly, but the adsorption capacity decreased gradually. When the adsorbent concentration was 0.2 g L^{-1}, the adsorption capacity Q_e was 242.2 mg g^{-1}, and the adsorption efficiency was 51.3%. When the adsorbent concentration was 0.4 g L^{-1}, the adsorption efficiency of TC was greatly improved to 53.7%, and the adsorption capacity was reduced to 134.2 mg g^{-1}. At 2 g L^{-1}, although the adsorption capacity was only 27.641 mg g^{-1}, the treatment efficiency reached 58.538%. This was because an excessive adsorbent dose provides too many adsorption sites, reducing the utilization rate and adsorption capacity of the adsorbent.[45] Considering the cost-effectiveness and the TC-removal performance of ANA, the ANA adsorbent concentration of 0.4 g L^{-1} was selected as one of the optimum concentrations.

The effect of different pH values on the adsorption of TC by ANA is shown in Fig. 5b. The highest adsorption rate of TC by ANA was 53.7% and the adsorption capacity Q_e was 134.2 mg g^{-1} at pH 7. Under alkaline conditions (pH 8–11), the adsorption capacity of the adsorbent ANA for TC gradually decreased with the increase in pH value, and the adsorption capacity decreased from 109.0 to 98.5 mg g^{-1}. In the solution system, TC is an amphoteric molecule, and its dissociation constants were 3.3, 7.7 and 9.7, respectively. When the pH value was lower than 3.3, the cationic form TCH$_3^+$ of TC became the main existing form in the solution. With the increase in pH value to 7.7, TC mainly existed in the form of TCH$_2^0$. When the pH value was further increased to above 9.7, the anionic forms TCH$^-$ and TC^{2-} became the dominant species.[46,47] Based on the zeta potential in Fig. 5c, the results show that ANA was negatively charged in the pH range of 3–11. The adsorption capacity of ANA to TC was weak, which may be attributed to the negative charge interaction between TC and ANA due to electrostatic repulsion when the pH value exceeded 8.

However, In the acidic environment (pH 3–6), the adsorption capacity of TC by the adsorbent ANA showed an upward trend with the increase in pH value, and its adsorption capacity increased from 41.8 to 53.75 mg g^{-1}. Therefore, under acidic conditions, ANA has a strong reduced adsorption capacity for TC. When the pH value decreased to 3, the removal efficiency was further reduced despite the competitive adsorption effect. This phenomenon could be attributed to the fact that under acidic conditions, the high concentration of H$^+$ and H$_3$O$^+$ in the system competes with TC for adsorption sites, resulting in a decreased adsorption capacity of ANA for TC with the decrease in pH value.[48] In addition, the silica–alumina structure of ANA
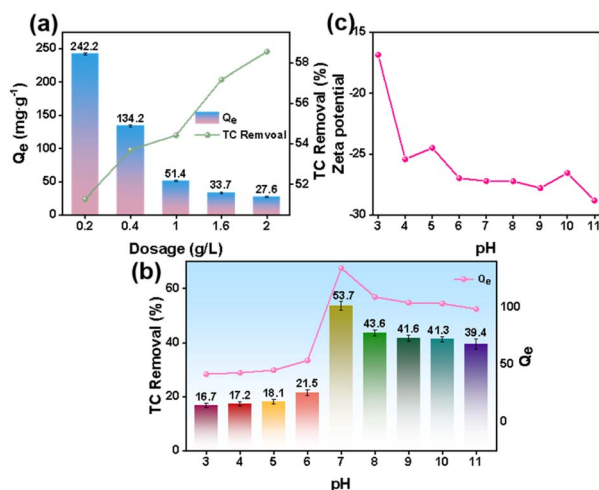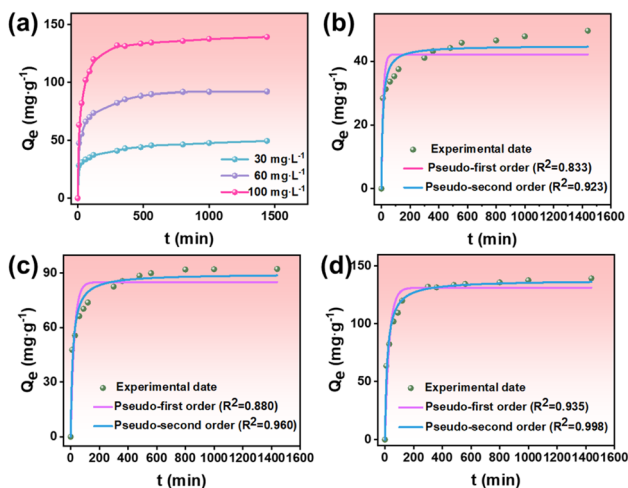
Fig. 6 Effect of concentration on the adsorption (a), pseudo-first-order kinetic model and pseudo-second-order kinetic model of 30 mg L^{-1} (b) 60 mg L^{-1} (c) and 100 mg L^{-1} (d) of TC.

may be damaged to a certain extent under lower pH conditions.[49] Therefore, the subsequent experiments were carried out by adjusting the pH to pH 7 to assess the solubility of the TC solution.

Adsorption kinetic study

Fig. 6a shows the adsorption kinetic curve of TC on ANA at 25 °C when the initial concentrations were 30, 60 and 100 mg L^{-1}, respectively. The adsorption of TC increased significantly at the initial stage, and the upward trend decreased after 200 min. The adsorption equilibrium of TC on ANA was reached at about 300 min. The adsorption process of TC by ANA could be divided into three stages: rapid adsorption in the early stage, slow adsorption in the middle stage and adsorption equilibrium in the later stage. At the initial stage of adsorption, there were a large number of free adsorption sites on the surface of ANA, and the concentration gradient between the surface and TC was the largest. TC molecules were rapidly transferred from the solution to the adsorption sites of ANA. With the progress of the adsorption process, the adsorption sites were gradually occupied by TC, and the repulsive force of the adsorbed TC molecules on the remaining TC molecules in the solution was enhanced, which led to a decrease in the adsorption rate of ANA, and then adsorption equilibrium was reached.[50]

The kinetic constants of the two models are listed in Table 4. The correlation coefficients of TC evaluated by the pseudo-first-

order kinetic model were 0.825–0.935, respectively. The calculated equilibrium adsorption capacity $Q_{e\ cal}$ (Table 4) was quite different from the experimental equilibrium adsorption capacity Q_e, indicating that the pseudo-first-order kinetic equation could not accurately describe the adsorption process. According to the pseudo-second-order kinetic model (Fig. 6 and Table 4), the correlation coefficients for the TC adsorption curves were 0.923–0.998, respectively. The calculated equilibrium adsorption capacity $Q_{e\ cal}$ value was in good agreement with the experimental equilibrium adsorption capacity Q_e value, and so the pseudo-second-order kinetic model was more suitable for describing the whole adsorption process of TC.[51]

Adsorption isotherm study

The adsorption isotherms of TC on ANA at 298.15 K and 308.15 K are shown in Fig. 7. With the increase in temperature, the adsorption equilibrium capacity of ANA increased, indicating that the adsorption of TC on ANA was an endothermic process.[52] As shown in Fig. 7, the adsorption properties of ANA for TC at 298.15 K and 308.15 K were analyzed by Freundlich, Langmuir and D–R adsorption isotherms. The Langmuir model represents single-layer adsorption at specific homogeneous sites,[53] while the Freundlich equation is suitable for multi-layer adsorption.[54] The Freundlich and Langmuir isothermal adsorption constant models are given in Table 5. The Freundlich equation constant $1/n$ for the ANA adsorption of TC was 0.309–0.474, indicating that the adsorption process was favorable. The correlation coefficient R^2 for the Langmuir isotherm model of TC was 0.930–0.962, and the correlation coefficient R^2 of the Freundlich isotherm model was 0.874–0.930, respectively. The adsorption isotherm of TC conformed to the Langmuir isotherm model, which is a single-layer adsorption. Next, R_L was determined to assess the adsorption capacity of ANA to TC, and it was found that $R_L < 1$ at the two temperature conditions, indicating that the adsorption was favorable.[55] The D–R model
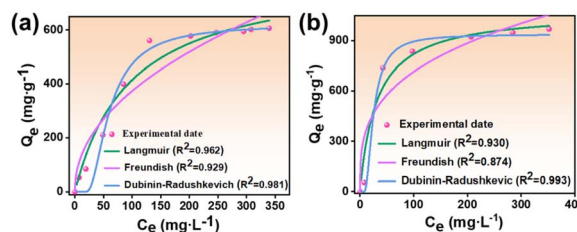

Fig. 7 Desorption isothermal adsorption models of TC at 298.15 K (a) and 308.15 K (b).

Table 4 Kinetic model constants for the adsorption of TC on ANA at different adsorbent concentrations

C_0 mg L^{-1}	Q_e mg g^{-1}	Pseudo-first-order			Pseudo-second-order		
		k_1 (min^{-1})	$Q_{e\ cal}$	R^2	k_2 ((g mg^{-1} min)$^{-1}$)	$Q_{e\ cal}$	R^2
30	49.6	0.079	42.17	0.826	0.00211	44.89	0.923
60	92.3	0.040	85.01	0.880	0.00073	89.66	0.960
100	134.2	0.033	131.21	0.935	0.00043	137.78	0.998

Table 5 Constants for the Freundlich and Langmuir isotherm equations for the adsorption of TC on ANA at different temperatures

T (K)	Langmuir model			Freundlich model			D–R model			
	Q_0	R_L	R^2	b	$1/n$	R^2	Q_m	K	E	R^2
298.15	816.3	0.0103	0.962	42.3	0.474	0.930	619.76	0.00044	33.71	0.981
308.15	1075	0.0321	0.930	172.0	0.309	0.874	936.86	0.000067	86.39	0.993

can be used to judge the adsorption types on the surface of ANA, and it was found that $E > 20$ kJ mol^{-1} under the two temperature conditions, indicating that the adsorption of ANA on TC occurred *via* chemical adsorption.[54]

Conclusions

The current research goal was to realize the recycling and resource utilization of waste by using BA to prepare analcime zeolite. BA from Xinjiang was used to synthesize analcime by an acid leaching–melting–hydrothermal method, and it was used to adsorb antibiotics (TC, CIP, NOR and ENR) in sewage. Compared with the existing literature, the hydrothermal synthesis temperature and time were lower. XRD and FT-IR characterizations proved that the ANA was pure analcime zeolite. In addition, no additional silicon source was required. The chemical-physical, morphological and spectral characterizations of the ANA proved the feasibility of the experimental scheme proposed in this paper. ANA displayed a flower-like and needle-like three-dimensional structure and the specific surface area was 20 m^2 g^{-1}. These prove that it had a certain adsorption potential. ANA was used to adsorb TC, CIP, NOR and ENR in water, and the adsorption capacities were 134.2, 64.3, 56.5 and 43.8 mg g^{-1}, respectively. It was found that ANA had a strong adsorption performance for TC, and so the adsorption process of TC was studied in detail. It was found that the optimal adsorbent dose was 0.4 g L^{-1}, pH 7, and the contact time was 300 min. The maximum adsorption capacity was 936.86 mg g^{-1}, which was much higher than the adsorption capacity of the existing zeolite for TC. The kinetic and isotherm fitting data showed that the adsorption of TC on ANA was mainly *via* monolayer chemical adsorption, and the process was more in line with the pseudo-second-order kinetic model and the Langmuir isotherm adsorption model. These results confirm that ANA is an efficient and economical TC adsorbent.

Data availability

All data supporting this study has been included in the article.

Conflicts of interest

There are no conflicts to declare.

Acknowledgements

References

1 H. Duan, Q. Huang, Q. Wang, B. Zhou and J. Li, *J. Hazard. Mater.*, 2008, **158**, 221–227.
2 J. Hong, S. Zhan, Z. Yu, J. Hong and C. Qi, *J. Cleaner Prod.*, 2018, **174**, 65–73.
3 E. Insa, M. Zamorano and R. López, *Resour. Conserv. Recycl.*, 2010, **54**, 1048–1059.
4 R. R. A. M. Mato and M. E. Kaseva, *Resour. Conserv. Recycl.*, 1999, **25**, 271–287.
5 H. Ezeala, O. C. Okeke, C. C. Amadi, M. O. Irefin, E. K. Okeukwu, T. C. Dikeogu and C. D. Akoma, *U.P. Eng. Res. J.*, 2023, **3**, 2782–8212.
6 Z. Ji and Y. Pei, *Chemosphere*, 2019, **225**, 579–587.
7 C. H. K. Lam, A. W. M. Ip, J. P. Barford and G. McKay, *Sustainability*, 2010, **2**, 1943–1968.
8 L. P. T. Mangialardi, G. Schena and P. Sirini, *Environ. Eng. Sci.*, 1998, **15**, 291–297.
9 E. Loginova, D. S. Volkov, P. M. F. van de Wouw, M. V. A. Florea and H. J. H. Brouwers, *J. Cleaner Prod.*, 2019, **207**, 866–874.
10 F.-Y. Chang and M.-Y. Wey, *J. Hazard. Mater.*, 2006, **138**, 594–603.
11 W. Zhu, P. J. Teoh, Y. Liu, Z. Chen and E.-H. Yang, *J. Cleaner Prod.*, 2019, **235**, 603–612.
12 L. Zhao, F.-S. Zhang, M. Chen, Z. Liu and D. B. J. Wu, *J. Hazard. Mater.*, 2010, **173**, 181–185.
13 Y. Huang, L. Wang, T. Wu, W. Liu and Q. Tang, *J. Cleaner Prod.*, 2023, **394**, 136355.
14 K. Yan, H. Sun, F. Gao, D. Ge and L. You, *J. Cleaner Prod.*, 2020, **244**, 118750.
15 J. Liu, Z. Li, W. Zhang, H. Jin, F. Xing and L. Tang, *J. Cleaner Prod.*, 2022, **337**, 130479.
16 R. Huang, P. Ding, D. Huang and F. Yang, *Lancet*, 2015, **385**, 773–774.
17 A. B. Ayobami, *Resour. Conserv. Recycl.*, 2021, **166**, 105351.
18 S. Gooi, A. A. Mousa and D. Kong, *J. Cleaner Prod.*, 2020, **268**, 121752.
19 A. S. Kumar, M. Muthukannan, K. Arunkumar, M. Sriram, R. Vigneshwar and A. G. Sikkandar, *Mater. Today: Proc.*, 2022, **66**, 2215–2225.
20 Z. Zhang, J. Wang, L. Liu, J. Ma and B. Shen, *Constr. Build. Mater.*, 2020, **254**, 119345.
21 K. Jagodzińska, K. Mroczek, K. Nowińska, K. Gołombek and S. Kalisz, *Energy*, 2019, **183**, 854–868.

22 B. M. Weckhuysen and J. Yu, *Chem. Soc. Rev.*, 2015, **44**, 7022–7024.

23 N. A. Rashidi and S. Yusup, *ACS Sustainable Chem. Eng.*, 2016, **4**, 1870–1884.

24 A. H. Ibrahim, X. Lyu and A. B. ElDeeb, *Nanomaterials*, 2023, **13**, 1091.

25 R. Gothwal and T. Shashidhar, *Clean: Soil, Air, Water*, 2014, **43**, 479–489.

26 A. K. Bhoi, A. Juneja and J. N. Mandal, *J. Cleaner Prod.*, 2023, **385**, 135763.

27 B. Lin and Y. Zhou, *Energy*, 2022, **241**, 122518.

28 J. Li, M. Gao, W. Yuan and J. Yu, *Chem. Sci.*, 2023, **14**, 1935–1959.

29 Q. Li, Y. Zhang, W. Gao and L. Cui, *Pet. Sci.*, 2010, **7**, 403–409.

30 F. Fotovat, H. Kazemian and M. Kazemeini, *Mater. Res. Bull.*, 2009, **44**, 913–917.

31 M. Yoldi, E. G. Fuentes-Ordoñez, S. A. Korili and A. Gil, *Microporous Mesoporous Mater.*, 2019, **287**, 183–191.

32 S. Lin, X. Jiang, Y. Zhao and J. Yan, *Sci. Total Environ.*, 2022, **851**, 158182.

33 D. Zhuang, Z. Chen and B. Sun, *Crystals*, 2025, **15**, 108.

34 D. Lia, Y. Chenb, J. Shena, J. Sub and X. Wuc, *Cem. Concr. Res.*, 2000, **30**, 881–886.

35 D. Novembre, C. Pace and D. Gimeno, *Mineral. Mag.*, 2018, **78**, 1209–1225.

36 A. Y. Atta, B. Y. Jibril, B. O. Aderemi and S. S. Adefila, *Appl. Clay Sci.*, 2012, **61**, 8–13.

37 D. Novembre and D. Gimeno, *Sci. Rep.*, 2021, **11**, 13373.

38 B. S. Liu, D. C. Tang and C. T. Au, *Microporous Mesoporous Mater.*, 2005, **86**, 106–111.

39 K. S. W. Sing and R. T. Williams, *Adsorpt. Sci. Technol.*, 2004, **22**, 773–782.

40 K. S. W. Sing, D. H. Everett, R. A. W. Haul, L. Moscou, R. A. Pierotti, J. Rouquerol and T. Siemieniewska, *Pure Appl. Chem.*, 1985, **57**, 603–619.

41 S.-N. Zhuo, T.-C. Dai, H.-Y. Ren and B.-F. Liu, *Bioresour. Technol.*, 2022, **359**, 127477.

42 J. Zhou, F. Ma and H. Guo, *Chem. Eng. J.*, 2020, **384**, 123290.

43 Y. Mei, J. Xu, Y. Zhan, B. Li, S. Fan and H. Xu, *Bioresour. Technol.*, 2021, **325**, 124732.

44 H. Huang, Z. Niu, R. Shi, J. Tang, L. Lv, J. Wang and Y. Fan, *Bioresour. Technol.*, 2020, **306**, 123096.

45 S. Meenakshi, C. S. Sundaram and R. Sukumar, *J. Hazard. Mater.*, 2008, **153**, 164–172.

46 X. Zhu, Y. Liu, F. Qian, C. Zhou, S. Zhang and J. Chen, *Bioresour. Technol.*, 2014, **154**, 209–214.

47 S.-N. Zhuo, T.-C. Dai, H.-Y. Ren and B.-F. Liu, *Bioresour. Technol.*, 2022, **359**, 127477.

48 R. Liu, L. Zou, Q. Huang, X. Cao and C. Yang, *J. Radioanal. Nucl. Chem.*, 2021, **329**, 103–113.

49 X. Du, X. Li, H. Zhang and X. Gao, *Chin. J. Catal.*, 2016, **37**, 316–323.

50 Y. Wang and L. Zhang, *J. Hazard. Mater.*, 2020, **395**, 22635.

51 P. Rożek, M. Król and W. Mozgawa, *J. Cleaner Prod.*, 2019, **230**, 557–579.

52 Q. Zhou, X. Jiang, Q. Qiu, Y. Zhao and L. Long, *Sci. Total Environ.*, 2023, **855**, 158741.

53 X. Fang, G. Zhang, X. Zhang, S. He, W. Xu, X. Zhang and S. Zhong, *Environ. Res.*, 2024, **258**, 119488.

54 J. Ma, Y. Lei, M. A. Khan, F. Wang, Y. Chu, W. Lei, M. Xia and S. Zhu, *Int. J. Biol. Macromol.*, 2019, **124**, 557–567.

55 M. J. Ahmed, B. H. Hameed and E. H. Hummadi, *Carbohydr. Polym.*, 2020, 247.